# Transient Space-Based GNSS Interference: Observations and Analysis

Zachary L. Clements and Todd E. Humphreys

Department of Aerospace Engineering and Engineering Mechanics, The University of Texas at Austin

## **BIOGRAPHIES**

Zachary L. Clements (B.S., Clemson University; M.S., University of Texas at Austin) is a P.h.D. candidate in the department of Aerospace Engineering and Engineering Mechanics at The University of Texas at Austin, and a member of the UT Radionavigation Laboratory. His research interests include statistical signal processing, detection, estimation, and software-defined radio, with an emphasis on GNSS interference detection, classification, and localization from Low Earth Orbit (LEO). He won the 2023 IEEE Walter Fried Award for best overall paper at the IEEE/ION PLANS.

Todd E. Humphreys holds the Ernest Dashiell Cockrell II Chair in Engineering in the department of Aerospace Engineering and Engineering Mechanics at The University of Texas at Austin. He is Director of the Wireless Networking and Communications Group and of the UT Radionavigation Laboratory. He specializes in the application of optimal detection and estimation techniques to problems in secure, collaborative, and high-integrity automated situational awareness. His awards include the National Science Foundation CAREER Award (2015), the Institute of Navigation Thurlow Award (2015), the IEEE Walter Fried Best Paper Award (2012, 2020, 2023), the Presidential Early Career Award for Scientists and Engineers (PECASE, via NSF, 2019), the Institute of Navigation Kepler Award (2023), and the Royal Institute of Navigation. He earned his B.S. and M.S. in Electrical and Computer Engineering from Utah State University, and his Ph.D. in Aerospace Engineering from Cornell University.

# **ABSTRACT**

This paper presents the analysis of a space-based Global Navigation Satellite System (GNSS) interference source responsible for multiple transient wide-area GNSS outage over Europe, Greenland, and Canada. Within the past decade, there has been a sharp increase in GNSS outages due to deliberate GNSS jamming and spoofing. An overwhelming majority of these cases can be traced to accidental leakage into the GNSS frequency bands, personal privacy devices, or electronic warfare spillover from nearby conflict zones. In contrast to the terrestrial or near-terrestrial sources responsible for most GNSS outages, this paper investigates GNSS interference source emanating from a spaced-based source. GNSS observables from a network of terrestrial-based GNSS reference stations are used to characterize the interference from 2019 to 2025. This paper offers three main contributions. First, it presents a detection framework for this type of interference. Second, it details the spatial and temporal patterns of wide-area GNSS outage events from the space-based interference source. Third, it presents satellite identification strategy to narrow down the number of candidate satellites.

## I. INTRODUCTION

Global Navigation Satellite Systems (GNSS) such as GPS provide meter-accurate positioning while offering global accessibility and all-weather, radio-silent operation. However, GNSS is fragile: its service is easily degraded by both deliberate (e.g., jamming and spoofing) and naturally occurring (e.g., multipath and atmospheric) interference [1]–[6]. The academic community has long warned the public about the threat of deliberate GNSS interference. Within the past five years, there has been no shortage of GNSS disruptions in aviation and maritime [6]–[9]. Fortunately, within the past decade, significant progress has been made in GNSS interference mitigation and countermeasures [4], [5], [10]–[14]. It has been shown that dedicated GNSS interference monitoring systems provide valuable spectrum situational awareness to enhance navigation security [15]–[17], with some demonstrating the ability to geolocate the interference source [18], [19]. Furthermore, GNSS receivers situated in LEO can provide unprecedented spectrum awareness, enabling terrestrial GNSS interference detection,

characterization, and geolocation with worldwide coverage [20]–[26]. Protecting the GNSS spectrum against interference is critical for safe navigation.

Networks of dedicated terrestrial-based GNSS receivers for GNSS monitoring are prevalent, as they serve many purposes: (1) GNSS satellite health monitoring, (2) corrections for precise point positioning, (3) atmospheric research, and (4) geodesy. The positions of these terrestrial reference stations are well-surveyed and the stations employ high-quality GNSS receivers that provide multi-constellation multi-frequency GNSS observables. Typically, these data products are used to monitor naturally occurring or accidental phenomena, such as atmospheric irregularities, ephemeris errors, and clock faults [27]–[29].

In addition to monitoring natural or accidental phenomena, terrestrial-based GNSS receiver networks can be repurposed to detect and characterize interference with a space-based origin. In 2021, a network of terrestrial reference stations was used to identify a Beidou satellite (NORAD ID 40749) as a source of interference in the B3I band (1268.52 MHz) [30], [31]. The offending satellite continuously transmitted tones centered at 1268.52 MHz, as well as  $\pm 10$  MHz and  $\pm 20$  MHz from 1268.52 MHz. These tones are no longer present at the time of writing. This was not the first time that a GNSS satellite caused unwanted interference in a GNSS band: it has been documented that GPS PRN 24 was for a time transmitting leakage tones at  $\pm 10$  MHz and  $\pm 20$  MHz from the GPS L5 frequency [32], but has since been fixed. Both of these events were likely due to faulty hardware onboard a GNSS satellite, resulting in a continuous transmission of interference.

This paper presents the detection, observation, and analysis of transient GNSS interference originating from a non-GNSS satellite. The phenomenon was briefly mentioned in [33]; this paper significantly extends on this work. Contrary to the GNSS interference detailed in [30]–[32], the interference in this paper is (1) transient—the duration of these interference events were less than 5 seconds, (2) affecting signals the GPS L1 frequency band, (3) causing drops in carrier-to-noise ratio of up to 10 dB, and (4) not originating from a GNSS satellite, assuming a single-satellite is the culprit. This interference was seen across a network of terrestrial reference stations operated by the International GNSS Service (IGS). The IGS reference station network collects and provides high-quality multi-GNSS observables that are freely available for scientific advancement and public benefit [34]–[37]. In this paper, the high-rate 1 Hz GNSS observables collected by the IGS stations are analyzed. These data were retrieved from the Crustal Dynamics Data Information System (CDDIS) archive, which is made available through NASA's archive of space geodesy data [38].

On multiple occasions, all tracked signals on the GPS L1 frequency at numerous IGS reference stations spanning Europe, Greenland, and Canada simultaneously saw a sudden brief drop in the carrier-to-noise ratio. The onset of the disruption is synchronized, which suggests a single source per disruption. The receivers are far enough apart that no single ground-based or aircraft-based source could reach them, hence the space-based origin hypothesis. Whether these interference events are malicious or not, the fact that radio frequency interference (RFI) events are generated in space yet not from GNSS satellites is a novelty and adds a new dimension to the challenge of GNSS security. This paper has three main contributions. First, it presents a detection framework for this type of interference. Second, it details the temporal and spatial properties of multiple wide-area GNSS outage events from the space-based interference source. Third, it presents a satellite identification strategy to reduce the number of candidate satellites.

# II. MEASUREMENT MODELS

The IGS reference station network collects and provides high-quality, multi-GNSS observables in the standardized Receiver Independent Exchange Format (RINEX) [37]. These GPS time-tagged observables include carrier phase, pseudorange, Doppler, and carrier-to-noise ratio (CNR) measurements for each tracked GNSS satellite. In this paper, the CNR observables from GPS L1 C/A signals at stations providing high-rate (1 Hz) GNSS observables will be analyzed. Let  $CNR^{ij}$  denote the true CNR from the ith station and jth GPS satellite.  $CNR^{ij}$  is expressed as

$$CNR^{ij} = P_R^{ij} - N_0^i \qquad (dB-Hz)$$
 (1)

$$P_{R}^{ij} = P_{T}^{j} + G_{T}^{j} \left(\theta_{T}^{ij}, \phi_{T}^{ij}\right) + G_{R}^{i} \left(\theta_{R}^{ij}, \phi_{R}^{ij}\right) + L^{ij}$$
 (dBW) (2)

where  $P_{\rm R}^{ij}$  is the received power at the ith station from the jth GPS satellite,  $N_0^i$  is the transmit power of the jth GPS satellite,  $G_{\rm T}\left(\theta_{\rm T},\phi_{\rm T}\right)$  is the transmitter's antenna gain pattern,  $G_{\rm R}\left(\theta_{\rm R},\phi_{\rm R}\right)$  is the receiver's antenna gain pattern,  $\theta$  is the off-boresight angle,  $\phi$  is the azimuth angle, and  $L^{ij}$  is the path loss between the ith station and the jth GPS satellite, defined as

$$L^{ij} = 20\log_{10}\left(\frac{\lambda}{4\pi\rho^{ij}}\right) \qquad (dB) \tag{3}$$

where  $\lambda$  is the carrier wavelength and  $\rho^{ij}$  is the range between the ith station and the jth GPS satellite.

The CNR is replaced by the carrier-to-interference-and-noise ratio (CINR) when there is an interference source present. Let CINR $^{ij}$  denote the true CINR between the ith station and jth GPS satellite. CINR $^{ij}$  is expressed as

$$\operatorname{CINR}^{ij} = P_{\mathrm{R}}^{ij} - 10\log_{10}\left(\tilde{N}_0^i + \tilde{I}_0^i\right) \qquad (\mathrm{dB-Hz}) \tag{4}$$

where  $\tilde{N}_0^i$  is the linear unit equivalent of the noise power density  $N_0^i$ , satisfying  $N_0^i = 10 \log_{10} \left( \tilde{N}_0^i \right)$ , and  $\tilde{I}_0^i$  is the linear unit equivalent of the interference power density  $I_0^i$ , satisfying  $I_0^i = 10 \log_{10} \left( \tilde{I}_0^i \right)$ .  $I_0^i$  is defined as

$$I_0^i = S_{\mathbf{I}}^i(0) \qquad (\mathsf{dBW/Hz}) \tag{5}$$

where  $S_{\rm I}(f)$  is the spectrum of the interference process I(t) satisfying  $S_{\rm I}(f)=10\log_{10}\left(\tilde{S}_{\rm I}(f)\right)$ , where  $\tilde{S}_{\rm I}(f)$  is defined as

$$\tilde{S}_{I}(f) = \tilde{S}_{c}(f) \star \tilde{S}_{r_{I}}(f + \hat{f}_{D})$$

$$\tag{6}$$

where  $\tilde{S}_{c}(f)$  is the spectrum of the local replica code,  $\tilde{S}_{r_{1}}(f)$  is the spectrum of the received interference signal,  $\hat{f}_{D}$  is the receiver's estimate of the desired signal's apparent Doppler frequency, and  $\star$  denotes the convolution operation.

Let the received interference signal's power  $P_1^i$  in dBW at the *i*th station be defined as

$$P_{\rm I}^i = P_{\rm I} + G_{\rm I} \left( \theta_{\rm I}^i, \phi_{\rm I}^i \right) + G_{\rm R}^i \left( \theta_{\rm R}^{i\rm I}, \phi_{\rm R}^{i\rm I} \right) + L^{i\rm I} \qquad (\text{dBW})$$

$$(7)$$

where  $P_{\rm I}$  is the transmitted interference power and  $G_{\rm I}\left(\theta_{\rm I},\phi_{\rm I}\right)$  is the interference source's antenna gain pattern. Additionally,  $\tilde{P}_{\rm I}^i$  is the linear unit equivalent of  $P_{\rm I}^i$ , satisfying  $P_{\rm I}^i=10\log_{10}\left(\tilde{P}_{\rm I}^i\right)$ .

For example, consider when  $\tilde{S}_{r_1}(f)$  is spectrally flat, is limited to a two-sided bandwidth B Hz, and the received power in the band  $\tilde{P}^i_1$  is spread uniformly across the whole received band. Then  $\tilde{I}^i_0$  takes the form

$$\tilde{I}_0^i = \frac{\tilde{P}_{\rm I}^i}{B} \qquad \text{(W/Hz)} \tag{8}$$

As another example, consider when the shape of  $\tilde{S}_{r_1}(f)$  is matched to  $S_c(f)$  for a pseudorandom binary spreading code with a chip interval of  $T_c$ , and centered at the center of the band. This model applies for the spreading codes of GPS L1 C/A and P(Y), L2 C and P(Y), and L5 I and Q. Then  $\tilde{I}_0^i$  takes the form

$$\tilde{I}_0^i = \frac{2}{3} T_c \tilde{P}_I^i \qquad (W/Hz) \tag{9}$$

Details on these and other interference models, including derivations, are found in [5].

At the kth time epoch, the receiver at the ith station reports  $z^{ij}[k]$ , which is either the measured  $\mathrm{CNR}^{ij}$  under nominal operating conditions (the null hypothesis  $H_0$ ), or the  $\mathrm{CINR}^{ij}$  under interference (the null hypothesis  $H_1$ ), for all tracked GPS L1/CA signals. The reported measurement  $z^{ij}[k]$  is modeled under  $H_0$  and  $H_1$  as

$$H_0: z^{ij}[k] = \text{CNR}^{ij}[k] + w^{ij}[k]$$
 (10)

$$H_1: z^{ij}[k] = \text{CINR}^{ij}[k] + w^{ij}[k]$$
 (11)

where  $w^{ij} \sim \mathcal{N}(0, \sigma_{ij}^2)$ , is zero-mean additive white Gaussian noise (AWGN), that models thermal noise, atmospheric effects, and other minor effects.

# III. DETECTION

One of the challenging aspects of this problem is determining if interference is present or not. The observables reported in the RINEX files do not have an indication flag of whether or not if the receiver is operating under  $H_0$  or  $H_1$ . A detection framework is need that detects the onset of interference at each station. When a GPS receiver suddenly transitions from  $H_0$  to  $H_1$ , there will be a drop in  $z^{ij}[k]$  because of the sudden injection of  $I_0$ . Therefore, the time-difference of  $z^{ij}[k]$  can be used to detect the onset of interference. For the kth time-epoch and ith station, let  $e^{ij}[k]$  denote the time-differenced measurement

$$\epsilon^{ij}[k] = z^{ij}[k] - z^{ij}[k - L] \tag{12}$$

where  $L \in \mathbb{N}$  is the index delay. Depending on if interference is present,  $\epsilon^{ij}[k]$  takes on a different model and distribution

$$H_0: \quad \epsilon^{ij}[k] = \operatorname{CNR}^{ij}[k] - \operatorname{CNR}^{ij}[k-L] + \tilde{w}^{ij}; \quad \epsilon^{ij}[k] \sim \mathcal{N}(0, 2\sigma_{ij}^2)$$
(13)

$$H_1: \quad \epsilon^{ij}[k] = \text{CINR}^{ij}[k] - \text{CNR}^{ij}[k - L] + \tilde{w}^{ij}; \quad \epsilon^{ij}[k] \sim \mathcal{N}(\mu_i, 2\sigma_{ij}^2)$$

$$\tag{14}$$

where for a sufficiently small L, the expected difference  $\mu_i$  in dB-Hz is

$$\mu_i = 10 \log_{10} \left( \frac{\tilde{N}_0^i}{\tilde{N}_0^i + \tilde{I}_0^i} \right) \tag{15}$$

and could be calculated if all of the parameters were known, but it is often the case that most parameters are unknown. Suppose at the kth epoch and ith station, the receiver is tracking  $J_{ik}$  GPS L1 C/A signals. The interference detection test statistic at the ith station,  $\Lambda^i[k]$ , is the average difference of all  $\epsilon^{ij}[k]$  at the kth epoch.

$$\Lambda^{i}[k] = \frac{1}{J_{ik}} \sum_{j=1}^{J_{ik}} \epsilon^{ij}[k] \tag{16}$$

Its distribution under  $H_0$  and  $H_1$  is

$$H_0: \quad \Lambda^i[k] \sim \mathcal{N}(0, \, \sigma_i^2)$$
 (17)

$$H_1: \Lambda^i[k] \sim \mathcal{N}(\mu_i, \sigma_i^2)$$
 (18)

A one-sided locally most powerful detection hypothesis test is applied because the values  $\{\mu_i\}$  under  $H_1$  are unknown [39]. The values  $\{\sigma_i^2\}$  are also unknown, but can be empirically estimated at each station using historical data. Once they are estimated, the detection threshold  $\nu^i$  for the *i*th station can be calculated for a constant false alarm rate (CFAR) hypothesis test to detect the onset of interference. For example, the distribution of  $\Lambda^i$  from a day under  $H_0$  for two stations, METG and WRST, are shown in Fig. 1. Both look approximately zero-mean Gaussian distributed. The variation of  $\sigma_i^2$  can be attributed to local noise, different receivers and antennas, and quantization of the observed CNR. The hypothesis test becomes

$$\Lambda^i[k] \underset{H_0}{\gtrless} \nu^i \tag{19}$$

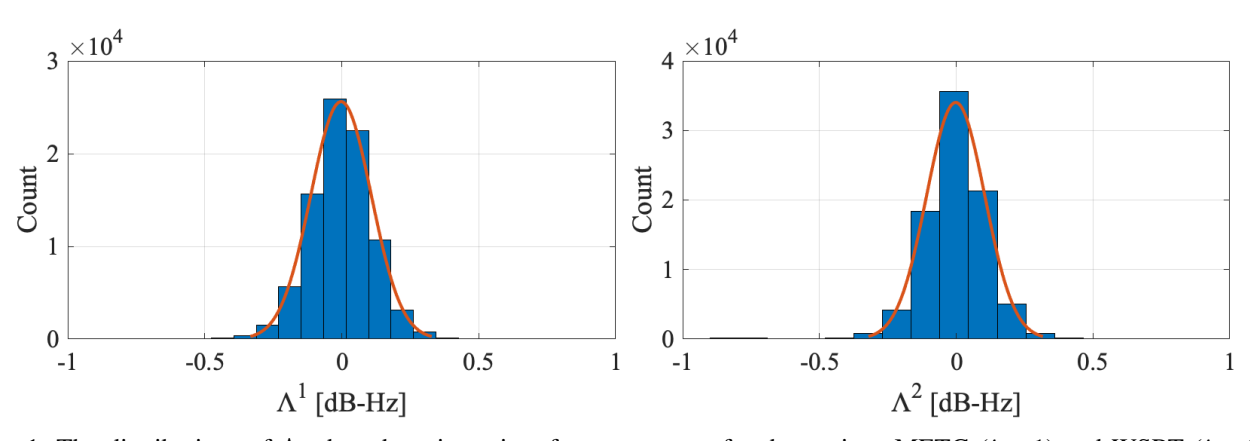


Fig. 1: The distributions of  $\Lambda$  when there is no interference present for the stations METG (i = 1) and WSRT (i = 2).

The rest of this section focuses on day 160 of year 2021. Fig. 2 shows the time history of  $z^{ij}$  and  $\Lambda^i$  over a 15 minute interval for four stations with L=3 seconds. The dashed red line indicates the detection threshold that corresponds to a probability of false alarm of 1e-4. Around the 700-second mark, interference was detected simultaneously at all four stations. While individual interference detections are not uncommon—reference stations occasionally experience local interference—what makes this event particularly noteworthy is the synchronized timing across geographically distant sites in Italy, Netherlands, Finland, and Greenland. Moreover, the interference exhibited the same characteristic signature at each location: a CNR drop lasting approximately 3 seconds. This strongly suggests that all four stations were affected by a common interference

source. Given the geographic spread, no terrestrial or airborne emitter could feasibly account for such simultaneous impact. Therefore, the source of interference must have been in orbit.

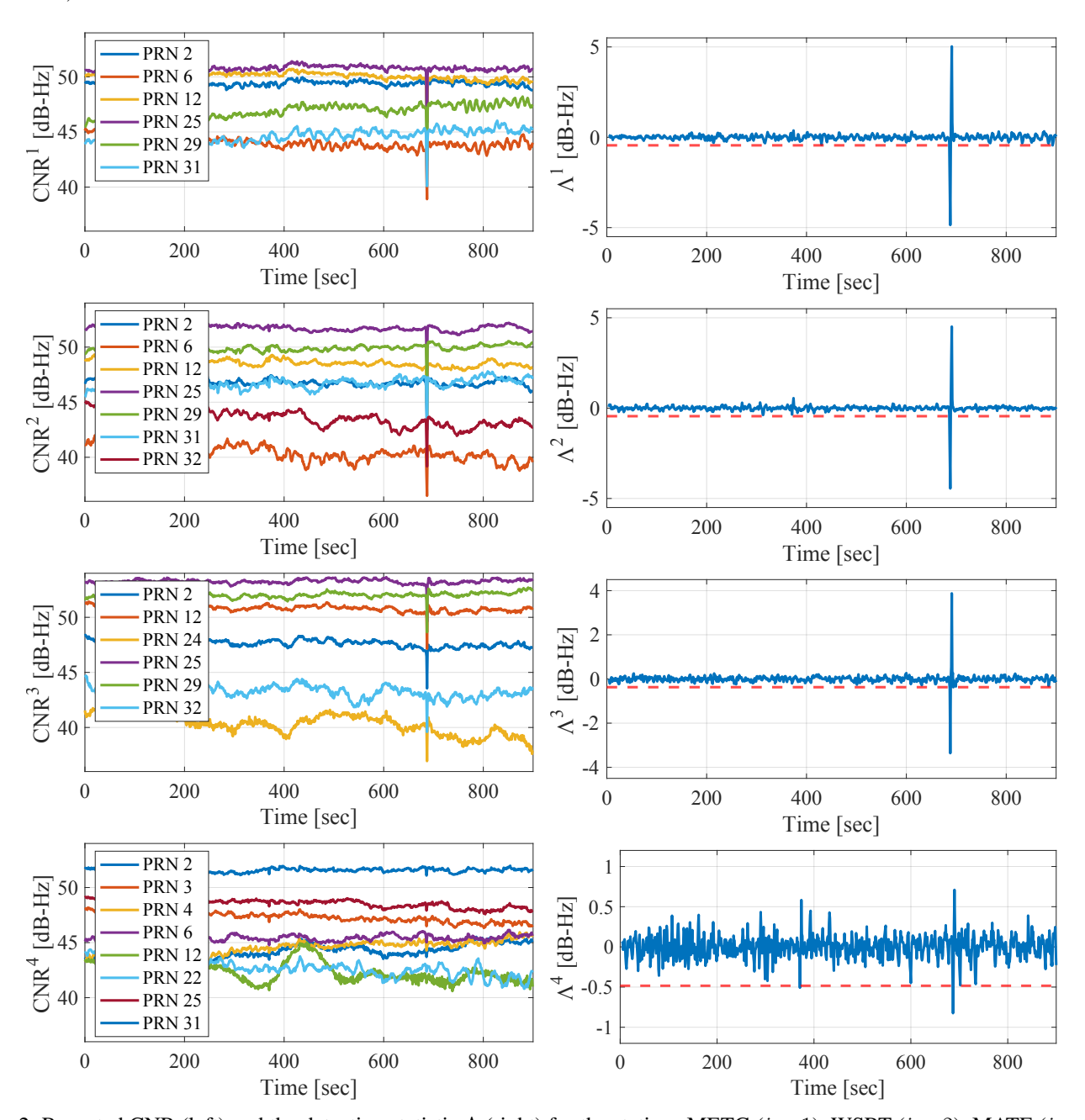


Fig. 2: Reported CNR (left) and the detection statistic  $\Lambda$  (right) for the stations METG (i=1), WSRT (i=2), MATE (i=3), and THU2 (i=4) over a 15 minute interval on day 160 of year 2021. The dashed red line is the detection threshold with a probability of false alarm of 1e-4.

The detection test was conducted continuously across multiple stations spanning Europe, Greenland, and Canada on day 160 of 2021. Fig. 3 illustrates the number of stations that triggered detections during this period with a probability of false alarm of 1e-4. Initially, the lower-power interference event was simultaneously detected by 21 stations, followed by the more powerful event simultaneously detected by 58 stations. This stronger interference event corresponds to approximately the 700-second mark shown in Fig. 2. The recorded CNR observables at each station align with the patterns depicted in Fig. 2, providing further evidence that these stations were affected by the same interference source. The heat map illustrating the

magnitude of the CNR drop is presented in Fig. 4. During the more powerful interference event, the tracked CNR of GPS L1 C/A signals exhibited drops as large as 6 dB-Hz, while the weaker event produced drops up to 1.5 dB-Hz.

The tracked Galileo E1 and BeiDou B1C/B1A signals also exhibited a concurrent drop in CNR, with the magnitude of the decrease at each station closely matching that observed in the GPS L1 signals. No corresponding CNR reductions were observed in GNSS signals on other center frequencies. This behavior is inconsistent with a solar radio burst, which typically exhibits broadband characteristics. Moreover, solar radio bursts evolve more slowly than the rapid onset observed in Fig. 3, and the associated CNR reduction typically persists for a longer duration. Therefore, this could not have been naturally occurring.

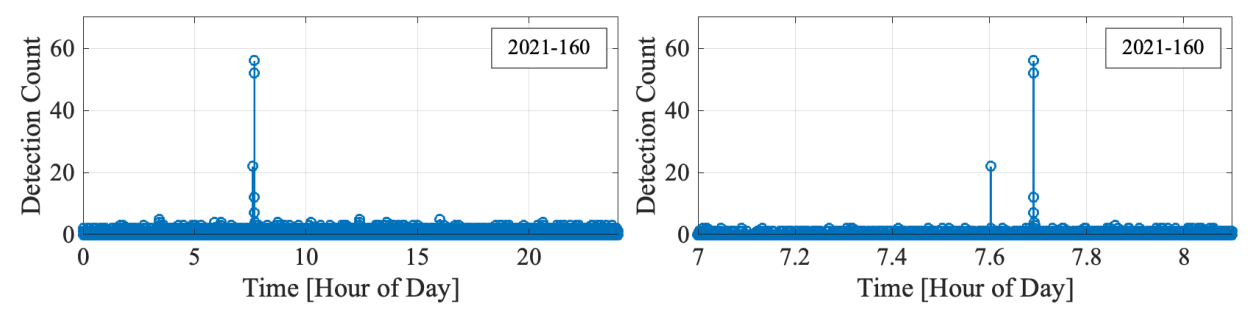


Fig. 3: The number of stations that detected interference during day 160 of year 2021. There was a lower-power interference event simultaneously detected by 21 stations, followed by a more powerful event that was simultaneously detected by 58 stations.

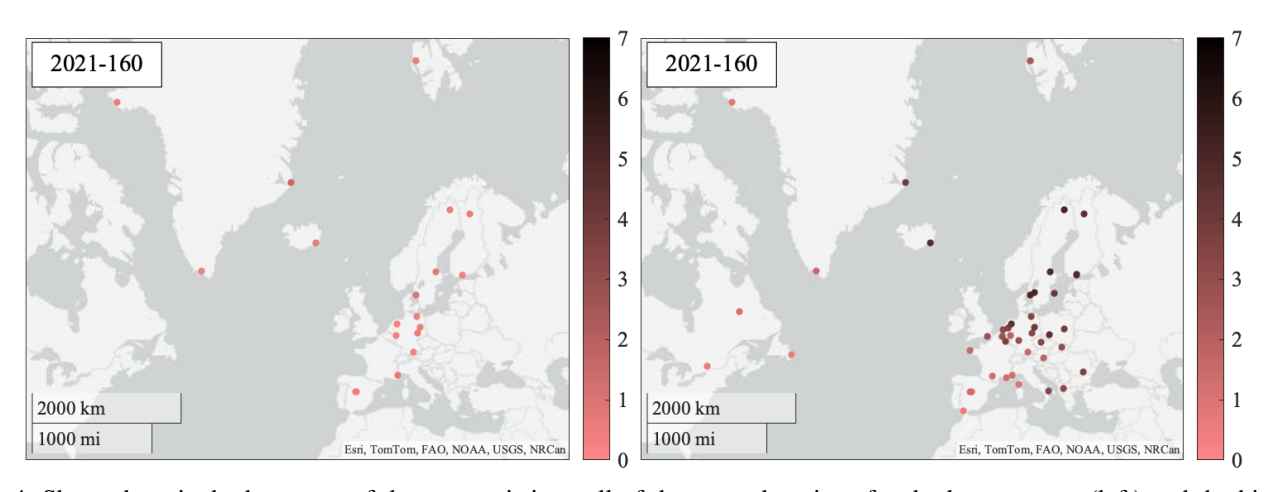


Fig. 4: Shown here is the heat map of the test statistic at all of the ground stations for the lower power (left) and the higher power (right) interference events. There was as large as a 6 dB-Hz drop in tracked CNR of GPS L1 C/A signals during the more powerful interference event, which was centered at the Baltics.

# IV. OBSERVATIONS

This sections details the transient space-based interference source's temporal and spatial patterns over a six year period.

# A. Temporal Patterns

High-rate data from over 165 reference stations collected over the past six years were retrieved and analyzed. The detection hypothesis test described earlier in this paper was applied to every station on a per-second basis starting from January 1, 2019. If interference was detected simultaneously at several stations, then an global detection is declared. A total of 72 days were identified with at least one wide-area transient GNSS interference event on the GPS L1 frequency, during which at least one station experienced a CNR drop of 5 dB-Hz or greater. The annual number of such occurrences is summarized

in Table I. The earliest detection of a significant wide-area interference event within this period occurred in October 2019; however, it is possible that similar events took place prior to 2019, though data availability and consistency were limited before this date.

	2019	2020	2021	2022	2023	2024	2025	Total
Count	8	17	5	7	15	9	11	72

TABLE I: The number of days per year that saw at least one wide-area transient GNSS interference on the GPS L1 frequency with at least one station seeing a drop of 5 dB-Hz or greater.

Fig. 5 presents the number of daily detections across three additional example days. Unlike Fig. 3, which shows a single high-power transient interference event, some days experienced multiple transient interference occurrences. Notably, day 146 of 2021 exhibited an interference signature similar to that of day 160 of the same year, with a lower-power burst followed by a high-power burst. This signature was observed on several other days. Days 204 of 2020 and day 014 of year 2025 recorded numerous high-power interference bursts. The timing of the bursts within a single day are typically periodic. The daily temporal patterns shown here of the high-power interference bursts are broadly representative of the phenomenon across all 72 days. There were approximately an additional 45 other days with weaker-power wide-spread transient interference events. On these days, the largest CNR drop did not exceed 5 dB-Hz. The weaker interference events are left out of this paper because they have a higher false alarm rate, but is still worth mentioning their existence.

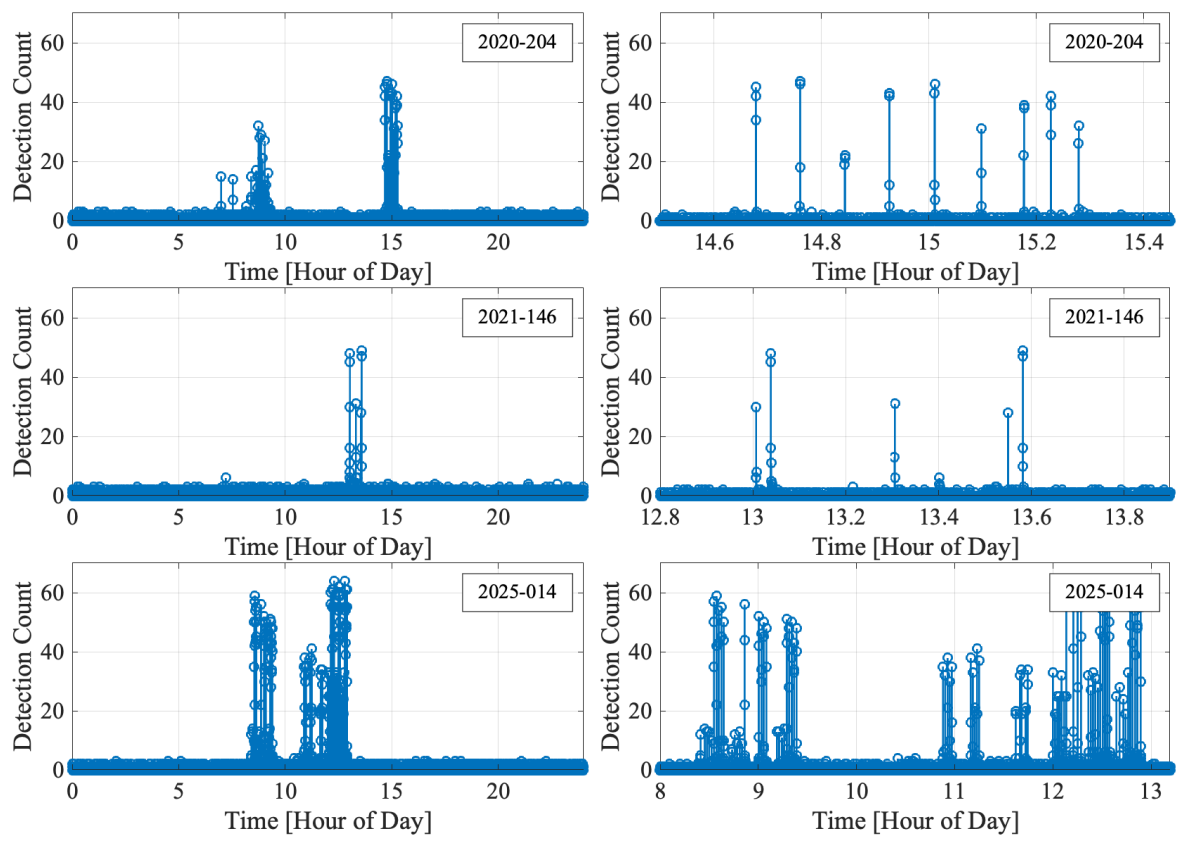


Fig. 5: Shown here are the number of stations that detected interference during three different days. Interference bursts can occur several times within a single day. The left column shows the entire day, while the right column is a zoomed in interval.

Fig. 6 presents a histogram showing the distribution of high-power interference bursts by day of the week and hour of the week. Notably, these interference bursts predominantly occurred during business days and business hours (UTC time). This temporal pattern suggests human involvement, as a purely random phenomenon would likely exhibit a more uniform

distribution. However, it still remains unclear whether these events were accidental or deliberate. If the days with only weaker interfernce are included, the distribution does not change.

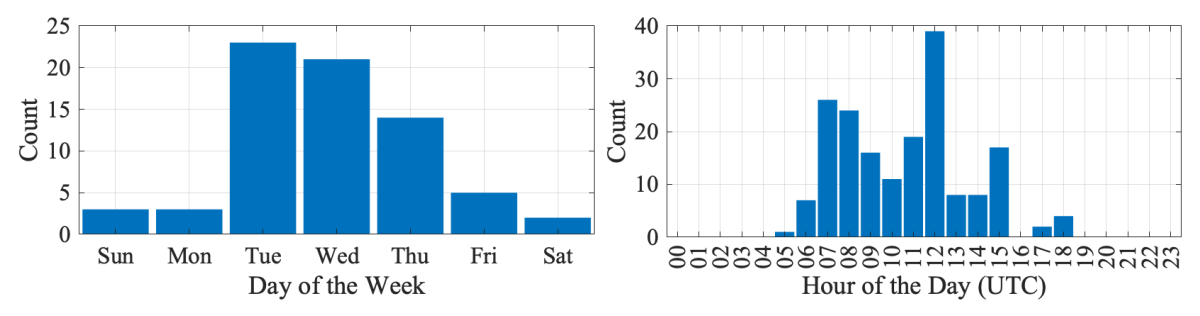


Fig. 6: Distribution of the day of the week and hour of day (with respect to UTC) that interference bursts with at least one station seeing a drop of 5 dB-Hz or greater occurred on. These high-power interference bursts typically occur during business days and business hours.

## **B. Spatial Patterns**

Across all 72 days, GNSS receivers in Europe were the most affected, with the Baltic region consistently experiencing the largest CNR drops. Fig. 7 shows example heat maps from day 146 of 2021 and day 014 of 2025. On day 146, two high-power interference bursts occurred, both producing nearly identical spatial patterns. Day 014 of 2025 saw multiple high-power bursts, all with consistent patterns matching the example shown. The largest CNR drop across all events was 10 dB-Hz recorded at the LAMA station in Poland in 2025. Notably, during wide-area interference events in Europe, no similar disruptions were detected elsewhere in the world.



Fig. 7: Interference heat maps for day 146 of year 2021 and day 014 of year 2025. GNSS receivers in the Baltic region are impacted the most, which is generally representative of nearly all of the interference events.



Fig. 8: Interference heat maps for day 204 of year 2020. This was one of the few days that showed a pronounced shift in the geographic center of the interference intensity.

Day 204 of 2020 exhibited a distinct interference pattern compared to other days. Fig. 8 presents heat maps corresponding to three (of the many) high-power interference bursts recorded on this day. The most severe impacts were observed in the

Baltic region (first image), Germany (second image), and the Nordic countries (third image). Notably, this was the only day that showed such a pronounced shift in the geographic center of interference intensity. This deviation may be attributed to satellite motion or to a change in the interference source's beam pointing vector.

#### V. BASIC SATELLITE IDENTIFICATION STRATEGY

One of the most fundamental approaches for identifying the potential interfering satellite is to determine which satellites were overhead the affected region during the time of the interference event. Two-Line Elements (TLEs) for publicly tracked orbiting objects can be obtained from space-track.org, a database maintained by the United States Space Force to support spaceflight safety. The TLEs can be used to compute the approximate position of an object at any given time. While the accuracy of these estimates degrades with the age of the TLE, the precision is more than sufficient for the purposes of this study.

Given knowledge of the positions of all publicly tracked satellites, a filtering strategy is implemented to reduce the number of candidate objects. The approach taken in this paper is to apply an elevation mask constraint across all stations that detected interference. For example, if it is assumed that the interference source maintained line-of-sight visibility to each affected station, a satellite must have been located above a 0° elevation angle—i.e., above the local tangent plane—at all stations during the event. By computing the tangent plane at each station, a feasible region can be constructed that satisfies the line-of-sight condition for all sites. Additionally, determining the minimum possible apogee of the interfering satellite can be formulated as an optimization problem.

Fig. 9 illustrates the positions of all tracked objects during the high-power interference burst on day 160 of 2021. It highlights the subset of satellites satisfying the  $0^{\circ}$  elevation mask constraint, excluding debris and rocket bodies. The red zone represents the feasible region in which the interfering satellite could have been located, and the red dot denotes the point corresponding to the minimum apogee the satellite could have been. For this event, the minimum apogee consistent with the elevation constraints is approximately 1,200 km. The number of satellites that satisfy many different elevation mask constraints during this day are shown in Table II.

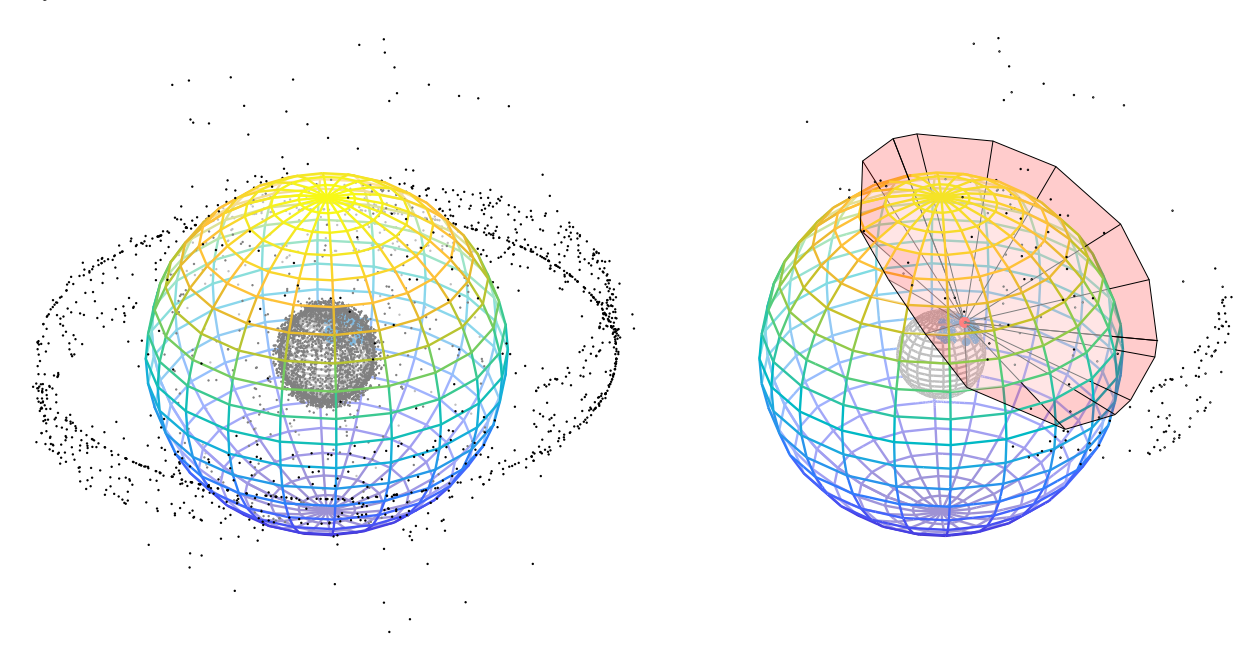


Fig. 9: Left: The position of all tracked objects during the high-power interference burst on day 160 year 2021. Right: The position of all satellites that satisfy a  $0^{\circ}$  elevation mask constraint and excluding all debris and rocket bodies. The red zone represents the feasible region the satellite could have been positioned. As a reference, the colored shell corresponds to Medium Earth Orbit (20,000 km altitude).

If it is assumed that a single satellite is responsible for the observed interference events, the list of candidate satellites can be further narrowed by identifying those that satisfy the elevation mask constraint across multiple events. The motion of

satellites across different days allows for the exclusion of many satellites, as their positions would not simultaneously meet the line-of-sight conditions at all affected stations.

For example, consider the high-power interference bursts on days 146, 160, and 337 of 2021. When a 0° elevation mask constraint is applied, only 13 satellites remain as viable candidates under the single-satellite assumption. Of these, three are in geostationary orbit, while the remaining ten are in highly elliptical (molniya) orbits. When this analysis is extended to include events on days 277 and 278 of 2019; days 209, 229, 299, 313, and 314 of 2022; and day 56 of 2025, only the same three geostationary satellites continue to satisfy the elevation mask constraint. Notably, these eleven days exhibit a recurring interference signature: a lower-power burst followed by a high-power burst. A summary of the satellites satisfying the multi-event elevation mask constraints is provided in Table II.

Interference Events	Elevation Mask					
Considered	-5°	-2.5°	$0^{\circ}$	$2.5^{\circ}$	5°	10°
2021(160)	400	311	226	175	131	103
2021(146, 160 337)	79	45	13	9	6	3
2019(277, 278), 2021(146, 160 337), 2022(209, 229, 299, 313, 314), 2025(56)	35	14	3	0	0	0

TABLE II: The table presents the number of satellites that satisfy various elevation mask constraints at all stations that detected interference on various days, under the assumption that a single satellite is responsible for the events.

#### VI. CONCLUSION

This paper presents a comprehensive analysis of wide-area transient GNSS interference from a space-based source affecting signals on the GPS L1 band. A detection framework was developed and used to identify these events within the 1 Hz CNR observables from over 165 IGS reference stations spanning 2019 to 2025. A total of 72 days were identified with at least one wide-area GNSS interference event, during which at least one station experienced a CNR drop of 5 dB-Hz or greater. Generally, GNSS receivers located near the Baltics are impacted the most. A geometric filtering method was introduced to constrain the set of possible satellites based on elevation masking. The observed timing patterns, which often coincide with business hours during weekdays, suggest a human-in-the-loop component, though the intent behind the interference remains unclear. Overall, this work provides strong empirical evidence of recurring, large-scale GNSS interference with a space-based origin and lays the foundation for further investigation into attribution and mitigation strategies.

#### VII. FUTURE WORK

This paper's conference presentation introduced several contributions that are not included in the current version of this paper: (1) a satellite association algorithm based on the Generalized Likelihood Ratio Test (GLRT), using the measured CNR drop at each station; (2) a framework for estimating receiver antenna gain pattern along with its associated uncertainty; and (3) a demonstration of the GLRT-based association technique using real CNR measurements on a parallel scenario. These contributions will be further developed and presented in a future publication.

#### **ACKNOWLEDGMENTS**

Research was supported by the U.S. Department of Transportation under Grant 69A3552348327 for the CARMEN+University Transportation Center, and by affiliates of the 6G@UT center within the Wireless Networking and Communications Group at The University of Texas at Austin.

#### REFERENCES

- [1] L. Scott, "Anti-spoofing and authenticated signal architectures for civil navigation systems," in *Proceedings of the ION GNSS Meeting*, pp. 1542–1552, 2003.
- [2] T. E. Humphreys, B. M. Ledvina, M. L. Psiaki, B. W. O'Hanlon, and P. M. Kintner, Jr., "Assessing the spoofing threat: Development of a portable GPS civilian spoofer," in *Proceedings of the ION GNSS Meeting*, (Savannah, GA), Institute of Navigation, 2008.
- [3] T. E. Humphreys, "Statement on the vulnerability of civil unmanned aerial vehicles and other systems to civil GPS spoofing," *United States House of Representatives Committee on Homeland Security: Subcommittee on Oversight, Investigations, and Management, July 2012.*
- [4] M. L. Psiaki and T. E. Humphreys, "GNSS spoofing and detection," Proceedings of the IEEE, vol. 104, no. 6, pp. 1258-1270, 2016.

- [5] T. E. Humphreys, "Interference," in Springer Handbook of Global Navigation Satellite Systems, pp. 469–503, Springer International Publishing, 2017.
- [6] G. S. Workgroup, "GPS spoofing: Final report of the GPS spoofing workgroup," tech. rep., OPSGROUP, 2024.
- [7] O. Osechas, F. Fohlmeister, T. Dautermann, and M. Felux, "Impact of GNSS-band radio interference on operational avionics," *NAVIGATION*, vol. 69, no. 2, 2022.
- [8] European Union Aviation Safety Agency, "Safety Information Bulletin 2022-02R3: Global Navigation Satellite System Outage and Alterations Leading to Communication / Navigation / Surveillance Degradation," July 2024. https://ad.easa.europa.eu/ad/2022-02R3.
- [9] E. P. Marcos, S. Caizzone, A. Konovaltsev, M. Cuntz, W. Elmarissi, K. Yinusa, and M. Meurer, "Interference awareness and characterization for GNSS maritime applications," in 2018 IEEE/ION Position, Location and Navigation Symposium (PLANS), p. 908–919, IEEE, April 2018.
- [10] A. Jafarnia-Jahromi, A. Broumandan, J. Nielsen, and G. Lachapelle, "GPS vulnerability to spoofing threats and review of antispoofing techniques," *International Journal of Naivgation and Observation*, pp. 1–16, 2012.
- [11] M. L. Psiaki and T. E. Humphreys, *Position, Navigation, and Timing Technologies in the 21st Century: Integrated Satellite Navigation, Sensor Systems, and Civil Applications*, vol. 1, ch. Civilian GNSS Spoofing, Detection, and Recovery, pp. 655–680. Wiley-IEEE, 2020.
- [12] K. Radoš, M. Brkić, and D. Begušić, "Recent advances on jamming and spoofing detection in GNSS," Sensors, vol. 24, no. 13, p. 4210, 2024.
- [13] D. Borio, C. O'Driscoll, and J. Fortuny, "GNSS jammers: Effects and countermeasures," in 2012 6th ESA Workshop on Satellite Navigation Technologies (Navitec 2012) & European Workshop on GNSS Signals and Signal Processing, pp. 1–7, IEEE, 2012.
- [14] Z. Clements, J. E. Yoder, and T. E. Humphreys, "Carrier-phase and IMU based GNSS spoofing detection for ground vehicles," in *Proceedings of the ION International Technical Meeting*, (Long Beach, CA), pp. 83–95, 2022.
- [15] S. Gunawardena, Z. Zhu, M. U. de Haag, and F. van Graas, "Remote-controlled, continuously operating GPS anomalous event monitor," *NAVIGATION*, vol. 56, no. 2, pp. 97–113, 2009.
- [16] S. Gunawardena and F. Van Graas, "Multi-channel wideband GPS anomalous event monitor," in Proceedings of the 24th International Technical Meeting of The Satellite Division of the Institute of Navigation (ION GNSS 2011), pp. 1957–1968, 2011.
- [17] J. Stader and S. Gunawardena, "Leveraging worldwide, publicly-available data to create an automated satnav interference detection system," in *Proceedings of the 2021 International Technical Meeting of The Institute of Navigation*, pp. 69–83, 2021.
- [18] J. A. Bhatti, T. E. Humphreys, and B. M. Ledvina, "Development and demonstration of a TDOA-based GNSS interference signal localization system," in *Proceedings of the IEEE/ION PLANS Meeting*, pp. 1209–1220, April 2012.
- [19] R. Mitch, M. Psiaki, and T. Ertan, "Chirp-style GNSS jamming signal tracking and geolocation," NAVIGATION, vol. 63, no. 1, pp. 15-37, 2016.
- [20] M. J. Murrian, L. Narula, P. A. Iannucci, S. Budzien, B. W. O'Hanlon, M. L. Psiaki, and T. E. Humphreys, "First results from three years of GNSS interference monitoring from low Earth orbit," *NAVIGATION*, vol. 68, no. 4, pp. 673–685, 2021.
- [21] D. M. LaChapelle, L. Narula, and T. E. Humphreys, "Orbital war driving: Assessing transient GPS interference from LEO," in *Proceedings of the ION GNSS+ Meeting*, (St. Louis, MO), 2021.
- [22] Z. Clements, P. Ellis, M. L. Psiaki, and T. E. Humphreys, "Geolocation of terrestrial GNSS spoofing signals from low Earth orbit," in *Proceedings of the ION GNSS+ Meeting*, (Denver, CO), pp. 3418–3431, 2022.
- [23] Z. Clements, P. Ellis, and T. E. Humphreys, "Dual-satellite geolocation of terrestrial GNSS jammers from low Earth orbit," in *Proceedings of the IEEE/ION PLANS Meeting*, (Monterey, CA), pp. 458–469, 2023.
- [24] Z. Clements, P. Ellis, and T. E. Humphreys, "Pinpointing GNSS interference from low Earth orbit," Inside GNSS, vol. 18, no. 5, pp. 42-55, 2023.
- [25] Z. Clements, I. Goodridge, P. Ellis, M. J. Murrian, and T. E. Humphreys, "Demonstration of single-satellite GNSS spoofer geolocation," in *Proceedings of the ION International Technical Meeting*, (Long Beach, CA), pp. 361–373, 2024.
- [26] Z. L. Clements, P. B. Ellis, M. J. Murrian, M. L. Psiaki, and T. E. Humphreys, "Single-satellite-based geolocation of broadcast GNSS spoofers from low Earth orbit," NAVIGATION, 2025. Submitted for review.
- [27] T. Walter, A. Hansen, J. Blanch, P. Enge, T. Mannucci, X. Pi, L. Sparks, B. Iijima, B. El-Arini, R. Lejeune, et al., "Robust detection of ionospheric irregularities," Navigation, vol. 48, no. 2, pp. 89–100, 2001.
- [28] T. Walter and J. Blanch, "Characterization of GNSS clock and ephemeris errors to support ARAIM," in Proceedings of the ION 2015 Pacific PNT Meeting, pp. 920–931, 2015.
- [29] R. Wang, Y.-F. Lai, J. Blanch, D. Akos, E. Phelts, and T. Walter, "Characterization of recent GPS satellite clock jumps," in *Proceedings of the 2024 International Technical Meeting of The Institute of Navigation*, pp. 226–240, 2024.
- [30] A. Patil, R. E. Phelts, Y.-H. Chen, S. Lo, and T. Walter, "Detecting space based interference on GNSS signals," in *Proceedings of the 36th International Technical Meeting of the Satellite Division of The Institute of Navigation (ION GNSS+ 2023)*, pp. 1232–1244, 2023.
- [31] A. Patil, R. E. Phelts, T. Walter, and S. Thoelert, "Detecting and localizing space based interference on GNSS signals using machine learning," in *Proceedings of the 2024 International Technical Meeting of The Institute of Navigation*, pp. 532–545, 2024.
- [32] J. York, A. Joplin, M. Bratton, and D. Munton, "A detailed analysis of GPS live-sky signals without a dish," *Navigation: Journal of The Institute of Navigation*, vol. 61, no. 4, pp. 311–322, 2014.
- [33] ESA NAVISP-EL3-014, "ĈĠI GNSS event notification service final presentation," 2023. https://navisp.esa.int/project/details/116/show.
- [34] J. M. Dow, R. E. Neilan, and C. Rizos, "The international GNSS service in a changing landscape of global navigation satellite systems," *Journal of geodesy*, vol. 83, pp. 191–198, 2009.
- [35] J. Kouba, "A guide to using international GNSS service (IGS) products," 2009.
- [36] O. Montenbruck, P. Steigenberger, L. Prange, Z. Deng, Q. Zhao, F. Perosanz, I. Romero, C. Noll, A. Stürze, G. Weber, et al., "The multi-GNSS experiment (MGEX) of the international GNSS service (IGS)-achievements, prospects and challenges," Advances in space research, vol. 59, no. 7, pp. 1671–1697, 2017.
- [37] G. Johnston, A. Riddell, and G. Hausler, "The international GNSS service," in Springer Handbook of Global Navigation Satellite Systems, pp. 967–982, Springer International Publishing, 2017.
- [38] C. E. Noll, "The crustal dynamics data information system: A resource to support scientific analysis using space geodesy," *Advances in Space Research*, vol. 45, no. 12, pp. 1421–1440, 2010.
- [39] H. L. Van Trees, Detection, Estimation, and Modulation Theory. Wiley, 2001.